ACS APPLIED NANO MATERIALS

Article

Cite This: ACS Appl. Nano Mater. 2019, 2, 6948−6959

www.acsanm.org

Controlled Nitrogen Doping of Graphene Quantum Dots through Laser Ablation in Aqueous Solutions for Photoluminescence and Electrocatalytic Applications

Rosemary L. Calabro, Dong-Sheng Yang,* and Doo Young Kim*

Department of Chemistry, University of Kentucky, Lexington, Kentucky 40506-0055, United States

Supporting Information

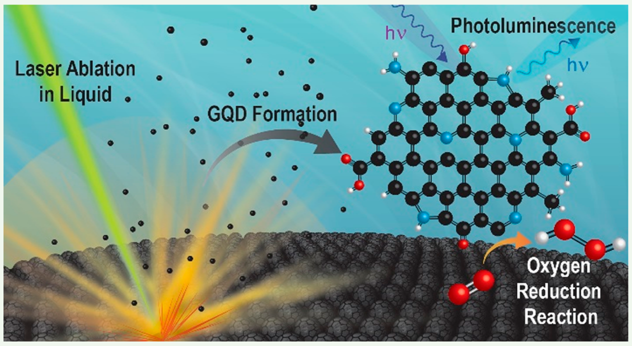

ABSTRACT: Nitrogen-doped graphene quantum dots (N-GQDs) have promising applications in catalysis and photoluminescence, but many existing synthetic methods require uses of harsh chemicals, long reaction times, and complicated purification steps and have poor control over the surface functional groups. Laser ablation in liquid (LAL) is a promising alternative method to prepare nanomaterials because of its fast production, use of fewer chemicals, simple purification, and fewer byproducts and its control of the product by precise tuning of laser ablation parameters. We report the use of LAL to produce N-GQDs from carbon nano-onions in aqueous solutions of ammonia, ethylenediamine, and pyridine. The choice of these dopants allowed for tuning the overall nitrogen content and the distribution of functional groups that led to the control over the photoluminescence emission wavelengths and lifetimes. High concentrations of amine groups tended to red-shift emission and exhibit shorter lifetimes, whereas pyridinic groups would blue-shift the emission and exhibit longer lifetimes. The N-GQDs also showed a promising performance as electrocatalysts for reducing oxygen to hydrogen peroxide, an important chemical widely used in industrial applications. The N-GQDs exhibited both low overpotentials and high selectivity for a two-electron oxygen reduction pathway.

KEYWORDS: *graphene quantum dots, laser ablation in liquid, photoluminescence, lifetime, oxygen reduction reaction, electrocatalysis*

INTRODUCTION

Graphene quantum dots (GQDs) are promising for many applications in sensing,[1,2] imaging,[3] photovoltaics, displays,[4] photodynamic therapy,[5,6] and catalysis.[7−9] GQDs have drawn special attention because they can be synthesized from cheap and abundant carbon sources in a large scale, avoid the use of heavy metals, and are lightweight as well as biocompatible.[10,11] Many of their applications are driven by their absorbance and photoluminescent (PL) properties with the goal of color control and high PL quantum yield (PLQY). While some previous work has suggested that the size of sp^2 carbon domains, termed intrinsic states, within a GQD could be used to control the absorbance and emission through quantum confinement effects,[12] others have demonstrated that defect states associated with functional groups present on the surface, often termed extrinsic states or molecule-like states, of GQDs, could govern the emission and increase the PLQY.[13,14] Therefore, by controlling the functional groups present on the GQDs, it is possible to tune the emission to the desired wavelength with improved PLQY.

Various research groups have demonstrated that the chemical state of oxygenated functional groups on GQDs has considerable influence on the emission. For instance, a high degree of chemical oxidation leads to a red shift in emission,[15] while chemical reduction of oxidized GQDs blue-shifts the PL.[16,17] Nitrogen doping has also been proven to have influence on the emissive properties of GQDs; however, there is still much debate on how various nitrogen functional groups affect the PL. Nitrogen can be present in various forms on GQDs including pyridinic, pyrrolic, amine, amide, graphitic, and nitro groups. One recent report shows a trend of enhanced PL with increased fractions of pyridinic nitrogen, while higher fractions of pyrrolic nitrogen have the opposite effects and favor nonradiative deactivations which decrease the PL.[18] Another shows that increased concentrations of graphitic nitrogen can red-shift the PL while also lowering the PLQY due to the introduction of midgap states that decrease the HOMO−LUMO gap.[19] This is attributed to the electron donating effect of the graphitic nitrogen into the intrinsic states of GQDs, but other types of nitrogen including pyridinic, pyrrolic, or amino groups did not have a similar effect.[20]

In contrast to the reports arguing for the role of nitrogen as dopants influencing HOMO−LUMO gap, other reports claimed that nitrogen doping could blue-shift the emission

Received: July 29, 2019
Accepted: October 7, 2019
Published: October 7, 2019

DOI: 10.1021/acsanm.9b01433
ACS Appl. Nano Mater. 2019, 2, 6948−6959

relative to undoped GQDs and this blue shift is attributed to a change in defect states and surface functional groups.[21] In fact, certain reaction conditions can allow the formation of molecule-like fluorophores that are attached to the GQDs and act as the primary emitting species.[22] For example, blue-shifted emission is observed with the introduction of a high fraction of pyridinic nitrogen,[23] while the red shifting of emission results from the increased concentration of amine groups.[24] Finally, samples containing higher overall nitrogen content have exhibited higher PLQYs when compared to similarly prepared samples with low nitrogen content.[25] Although the role of dopants in photoluminescence is not fully understood, it is clear that controlling both the ratios of the functional groups and the overall nitrogen content could influence the optical properties of the GQDs.

GQDs have been prepared through many top-down methods, such as chemical exfoliation, hydrothermal synthesis, and electron beam lithography, and by bottom-up methods, such as stepwise organic synthesis and pyrolysis of carbon precursors.[10,11,26,27] However, these methods suffer from limitations of multiple steps for preparation, low production yields, use of many hazardous chemicals, long purification processes, and production of nonuniform samples in both size and morphology. Pulsed laser ablation in liquid (LAL) has recently been proven as an alternative single-step method to produce various carbon nanomaterials including GQDs.[28−32] Potentially, LAL can overcome many of the limitations of other synthetic methods because it uses fewer chemicals, produces higher yields of desired products with few byproducts, and simplifies purification processes.[33−36] Typically, pulsed laser irradiation is incident on a target, generating plasma plumes that expand in liquid. The plasma is subsequently cooled by the surrounding liquid.[37] The presence of dopant molecules in the surrounding liquid allows for the inclusion of various heteroatoms and functional groups.[38] Nitrogen doping in particular has been achieved by laser ablation of carbon precursors with dopants including diethylenetriamine,[39] aminotoluene,[40] or urea.[41] It has been reported that an increase in laser power can induce a red shift in emission[40] and that nitrogen content can be controlled by varying the dopant concentration in liquid.[41] To the best of our knowledge, however, there are no reports on how the choice of nitrogen precursors in LAL would influence the distribution of nitrogen functional groups and the photoluminescence of the produced GQDs.

The oxygen reduction reaction (ORR) is an important reaction for energy conversion, biological respiration, and industry applications. ORR can occur through four- and two-electron processes that result in the production of water and hydrogen peroxide, respectively, in acidic environments.[42] While the four-electron process is important for the overall efficiency of fuel cells, the two-electron process is receiving an increased attention due to its efficient production of hydrogen peroxide. Hydrogen peroxide is an important chemical in many industrial applications including medical, environmental, food and beverage, cosmetics, paper making, and chemical synthesis.[43,44] Current methods to produce hydrogen peroxide, the anthraquinone process or direct synthesis from H_2 and O_2 gas, require multiple steps or involve dangerous reactions.[43] The implementation of the electrocatalytic ORR to produce hydrogen peroxide offers several advantages such as the availability of abundant and clean precursors, few, if any, purification steps, and safer production. The thermodynamic potential for the ORR to form peroxide is 0.76 V vs reversible hydrogen electrode (RHE),[45] and it is highly desirable to develop an efficient catalyst that is capable of reducing oxygen to hydrogen peroxide through the dominant two-electron process with low overpotential. Platinum has been shown to catalyze the ORR with low overpotential; however, it is expensive, susceptible to corrosion and CO poisoning, and only active for the four-electron process without modification.[44] GQDs address some of these limitations as they are produced from cheap and abundant precursors and are lightweight, and their catalytic properties can be tuned by doping with heteroatoms.[9,23] However, challenges remain to be addressed regarding the efficient scale up of catalysts with enhanced tolerance against surface deactivation by byproducts and impurities.

We report the synthesis of nitrogen-doped GQDs (N-GQDs) through LAL of carbon nano-onions (CNOs) in water along with the characterization of the PL and electrocatalytic properties of the LAL-prepared N-GQDs in comparison with LAL-prepared undoped GQDs. The nitrogen functional groups of the GQDs were tuned by use of different nitrogen containing precursors dissolved in water, including ammonia (N_A-GQDs), ethylenediamine (N_E-GQDs), and pyridine (N_P-GQDs). These N-GQDs were compared to GQDs that were produced in water without any nitrogen precursor molecules (Ox-GQDs). In general, N-GQDs with high fractions of pyridinic groups tended to favor blue emission, while amine groups resulted in a red-shifted emission. These N-GQDs showed high catalytic selectivity for the two-electron ORR process with the N_P-GQDs having the best performance. LAL demonstrated the single-step, fast, and clean production of the N-GQDs with few byproducts and tunable PL. LAL is a novel synthetic approach to produce clean electrocatalysts without surface contamination of active sites by using fewer chemicals and a simple synthetic step.

■ EXPERIMENTAL SECTION

Materials. Ammonia hydroxide (ACS 28.0−30.0% NH_3) was purchased from Alfa Aesar, ethylene diamine (≥99.5%) from Sigma-Aldrich, and pyridine (≥99.0%) from EMD Millipore. Nanodiamond (98+%, 6 nm diameter) powders were purchased from Nanostructured Amorphous Materials Inc. Potassium hydroxide (ACS grade) was purchased from VWR Analytical, a Nafion dispersion (D520, alcohol based 1000 equiv weight at 5 wt %) from FuelCellStore, acetylene carbon black (100% compressed) from Strem chemicals, Inc., and 20% Pt on Vulcan XC-72 (fuel cell grade) from Premetek Co. All chemicals were used without further purification. Deionized water was obtained from a Barnstead E-Pure ultrapure water purification system. Iso-Disk filters (PTFE 25-4 25 mm × 0.45 μm) were purchased from Supelco Inc.

Sample Preparation. *Preparation of CNOs.* CNOs were obtained by thermally annealing detonation nanodiamonds in a graphitization furnace under helium flow at 1650 °C for 1 h.

LAL Synthesis of GQDs. The LAL to produce GQDs was carried out similarly to our previously reported procedure.[32] In a typical setup an amount of about 50 mg of CNOs was pressed into a pellet at 10 000 psi and kept under pressure for 15 min. The pellet was transferred to a small vial, and 3 mL of liquid was added. The vial was placed in a larger secondary container with a quartz lid to prevent evaporation. The reaction container was placed on a rotating stand. The laser beam from a Quanta-Ray Lab 170 series Nd:YAG Q-switched laser was directed to the pellet using a prism and focused on the pellet surface using a lens. The laser power after passing through the prism and lens was measured to be 80% of the power before the optics. The pulse width was 6−8 ns and the repetition rate was 50 Hz. The pellet was irradiated for 1 h with 532 nm light at 100 mJ/pulse (measured before the prism) with the focal spot size of 1.5 mm diameter on the CNO target. After accounting for power loss due to focusing optics, this laser power and spot size result in a laser fluence of 4.5 J/cm^2. DI water was used to prepare Ox-GQDs; 2.5 M solutions of ammonia, ethylenediamine, and pyridine were used to prepare N_A-GQDs, N_E-GQDs, and N_P-GQDs, respectively. Following the laser ablation, the solution was filtered with a 450 nm syringe filter to remove any unconverted CNO pellet and dried overnight in an 80 °C oven to remove the liquid. The collected GQDs were redistributed in DI water prior to analysis.

Characterization Details. PL spectra were collected with a Horiba Scientific Fluoromax Plus-C fluorometer using 2 nm entrance and exit slits and an integration time of 0.1 s for both excitation and emission scans. PL lifetime measurements were performed using a DeltaHub high throughput time correlated single photon counting (TCSPC) controller and a NanoLED-390 pulsed excitation source (excitation wavelength 393 ± 10 nm). TCSPC measurements were collected at 425 and 465 nm emission with 5 nm bandpass at a repetition rate of 1 MHz over a measurement time of 200 ns. The instrument response function (IRF) was determined by measuring the scattering of the excitation source with a Ludox sample. Lifetime fitting was done using Horiba Scientific decay analysis software DAS6. Ultraviolet−visible (UV−vis) absorption spectra were obtained from a Thermo Scientific Evolution 201 UV−visible spectrophotometer at a scan rate of 600 nm/min and an integration time of 0.1 s. Fourier-transform infrared (FT-IR) spectra were obtained with a Thermo Scientific Nicolet iS50 FT-IR Spectrometer equipped with a diamond attenuated total reflectance (ATR) plate. To collect each spectrum a small (<10 μL) drop of highly concentrated GQD solution was placed on the ATR plate and was dried for 20 min in a 40 °C oven. Each spectrum was collected using 64 scans and a resolution of 4 cm^{-1}. X-ray photoelectron spectroscopic (XPS) measurements were conducted with a Thermo Scientific K-Alpha X-ray photoelectron spectrometer system using an aluminum Kα X-ray source. Samples were drop cast on a silicon wafer. A flood gun was used during analysis. The spot size of X-ray was about 400 μm. XPS survey spectra were obtained with five scans, and C 1s and N 1s XPS high resolution spectra were obtained with 10 scans. For transmission electron microscopy (TEM), 0.5 mg/mL solutions of GQDs were sonicated for 1 h, and then an amount of 10 μL of the solutions was drop cast on Lacey carbon 300-mesh copper grids. TEM images were obtained using a Thermo Scientific Talos F200X scanning/transmission electron microscope. Particle size analysis was carried out using the open source ImageJ software package. Atomic force microscopy (AFM) measurements were obtained using a Bruker Dimension Icon scanning probe microscope.

Electrochemical Measurements. All electrochemical measurements were performed in a 0.1 M KOH solution using a CHI-760D potentiostat with a Ag/AgCl electrode as the reference electrode, a Pt wire coil as the counter electrode, and a ring disk electrode (4 mm glassy carbon disk, 1 mm Pt ring) as the working electrode. For the working electrode, a GQD/carbon black composite was prepared in a 1:2 ratio. A solution containing 1 mg/mL composite with 0.5 wt % nafion binder in water was prepared and sonicated for 1 h. Following sonication, 10 μL of the solution was drop cast on the glassy carbon disk of the ring-disk electrode and allowed to dry in a 50 °C oven overnight. A N_2 or O_2 saturated environment was produced by bubbling the corresponding gas in the KOH solution for 30 min. For a typical sample cyclic voltammetry (CV) scans were collected in both N_2 and O_2 saturated environments. CV scans were collected in the scan range 1.26 to −0.24 V (vs RHE) at a scan rate of 20 mV/s. Rotating disk electrode (RDE) linear sweep voltammetric (LSV) measurements were collected in an O_2 saturated environment in the scan range 1.26 to −0.24 V (vs RHE) at a scan rate of 5 mV/s at rotation speeds ranging from 400 to 3200 rpm in increments of 400 rpm. Rotating ring disk electrode (RRDE) measurements were performed in an O_2 saturated environment at 1600 rpm in the scan range 1.26 to −0.24 V (vs RHE) at a scan rate of 5 mV/s, and a constant potential of 0.35 V was applied to the ring to detect any generated hydrogen peroxide. All samples were analyzed in the potential range of 1.26 to −0.24 V except for the Pt/C electrode which was analyzed in the potential range 1.26 to 0.06 V.

■ RESULTS

Figure 1a presents a schematic representation of a typical laser ablation setup. In general, a 532 nm pulsed nanosecond laser beam is directed through a prism and focused onto the pellet using a lens. Once the laser interacts with the CNO target (Figure 1b), a dense plasma of fragments from the precursor and carbon atoms is formed and then expands. Subsequently, the plasma is cooled by the surrounding liquid.[37] As the plasma cools, it nucleates and reacts with the water, and nitrogen containing solutes are dissolved in water, allowing for incorporation of various functional groups such as hydroxyl, carbonyl, and carboxyl oxygen groups and pyridinic, amine, pyrrolic, and graphitic nitrogen groups (Figure 1c). By focusing of the laser pulse on the CNO pellet, further laser pulses have minimal interactions with the formed GQDs that are in the solutions. The GQDs also have negligible

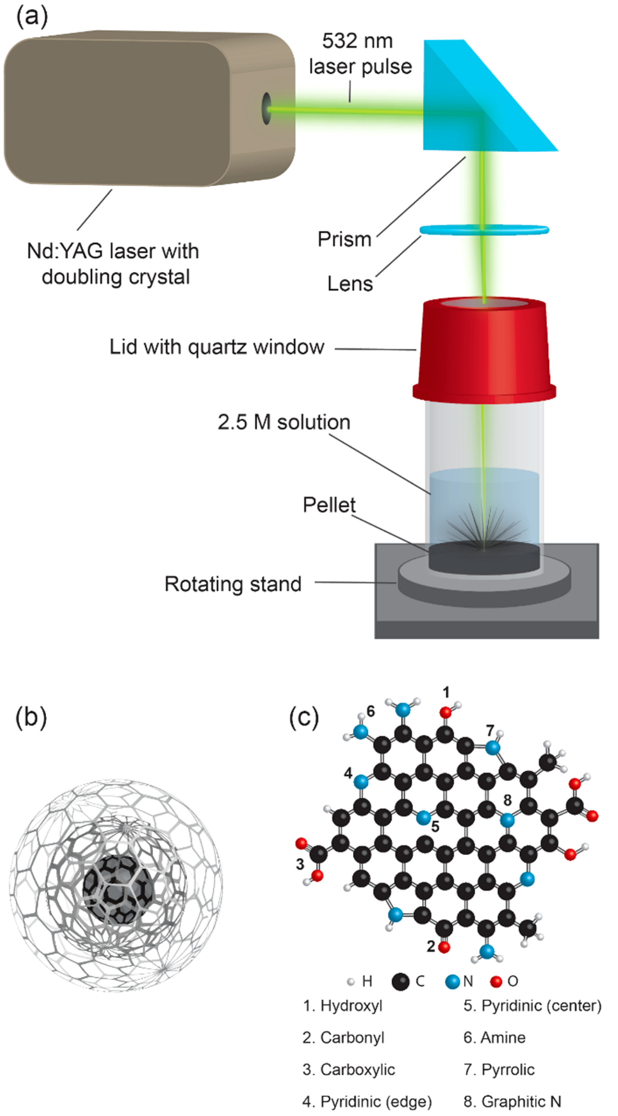

Figure 1. Schematic representation of a typical laser ablation setup (a). Upon laser irradiation, the precursor CNOs (b) are converted into graphene quantum dots (c).

absorbance at 532 nm which further minimizes interactions of the GQDs with the laser pulses. TEM images of the Ox-GQDs and N-GQDs are presented in Figure 2, and histograms of their particle size analysis are reported in Figure S1. The Ox-GQDs showed the presence of isolated particles (Figure 2a, inset), and most particles formed agglomerates due to their hydrophobicity. However, the small particles on the nanoscale were visible within the agglomerates. The Ox-GQDs have a much smaller particle size with an average diameter of 4.0(9) nm, while the N doped samples (Figure 2b−d) have particle diameters of 14(4) nm, 14(3) nm, and 15(4) nm for N_A-GQDs, N_E-GQDs, and N_P-GQDs, respectively. All four samples have similar size distributions with relative standard deviations of 20−25%, indicating that the choice of dopant does not greatly affect the size uniformity. AFM measurements are detailed in Figure S2 and show particle heights of 2.2(8) nm for Ox-GQDs, 6(2) nm for N_A-GQDs, 5.1(15) nm for N_E-GQDs, and 3.7(13) nm for N_P-GQDs, indicating that the lateral dimensions for all GQD samples are larger than their heights and that Ox-GQDs are in general smaller than the N-GQDs. The production yield was also considered by comparing the mass of produced GQDs to the mass of consumed CNOs. In a typical LAL experiment 53(7)% of the consumed CNOs are converted to GQDs while the remaining consumed pellet was filtered out of the solution. Future implementation of methods to recover and reuse the large filtered fragments of CNOs can be used to further improve the production yield.

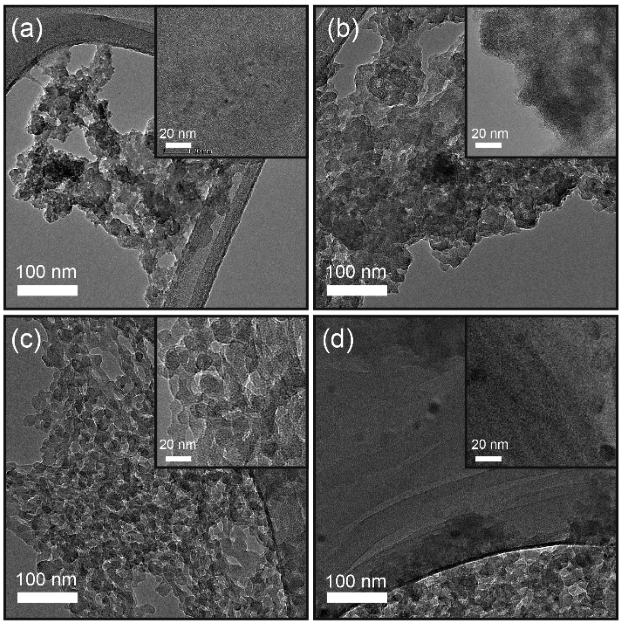

Figure 2. TEM images of the Ox-GQDs (a) and N-GQDs produced with ammonia (b), ethylenediamine (c), and pyridine (d). The scale bar for the larger images is 100 nm, and the scale bar for the insets is 20 nm.

The choice of the nitrogen precursor solutes had an influence on the functional groups formed on the nitrogen doped GQDs. The FT-IR spectrum of each sample is presented in Figure 3. The spectrum of the Ox-GQDs shows a broad peak with the maximum around 3400 cm^{-1} and several narrow ones in the region below 2000 cm^{-1}. The 3400 cm^{-1} peak is attributed to the hydrogen-bonded O−H stretching of hydroxyl functional groups, the 1700 cm^{-1} shoulder to the C═O stretching from carboxylic groups or ketones, the 1600 cm^{-1} peak to the aromatic ring stretch of the sp^2 hybridized carbon domains within the GQDs, the 1375 cm^{-1} peak to a CH_3 bend, and the 1150 cm^{-1} one to a sp^3 bonded C−O stretch. The spectra of the N_A-GQDs have a similar absorption profile as that of the Ox-GQDs. However, the peak in the O−H stretching region is much broader and shifted toward 3300 cm^{-1}, suggesting the presence of an amine N−H stretch. A new, strong peak appears at 1350 cm^{-1} due to an aryl C−N stretch,[46] and the sp^3 bonded C−O peak at 1150 cm^{-1} is split into two due to the additional presence of a sp^3 bonded C−N stretch. For both N_E-GQDs and N_P-GQDs, the amine N−H stretch at 3250 cm^{-1} is stronger relative to the O−H stretching, which is present as a shoulder, and the C−H stretching associated with the sp^2 and sp^3 carbons is more sharply defined at 3050 and 2950 cm^{-1}, respectively. Similar to the N_A-GQDs, the N_E-GQDs and N_P-GQDs show the N−H stretch, aromatic ring stretching, aryl C−N stretching, and sp^3 bonded C−N and C−O stretching in the 700−1700 cm^{-1} range;[46] however, the relative intensities are different for each sample. For the N_E-GQDs and N_P-GQDs the sp^3 bonded C−N and C−O stretching peaks become less resolved and much weaker, and the aryl C−N stretch is also suppressed. Moreover, the spectra of these two nitrogen-doped GQDs show an additional sharp, strong peak at 1670 cm^{-1} which can be assigned to the N−H bend, and the spectrum of the N_P-GQDs exhibits a large intensity increase of the aromatic ring stretch peak at 1600 cm^{-1} compared to those of the other GQDs.

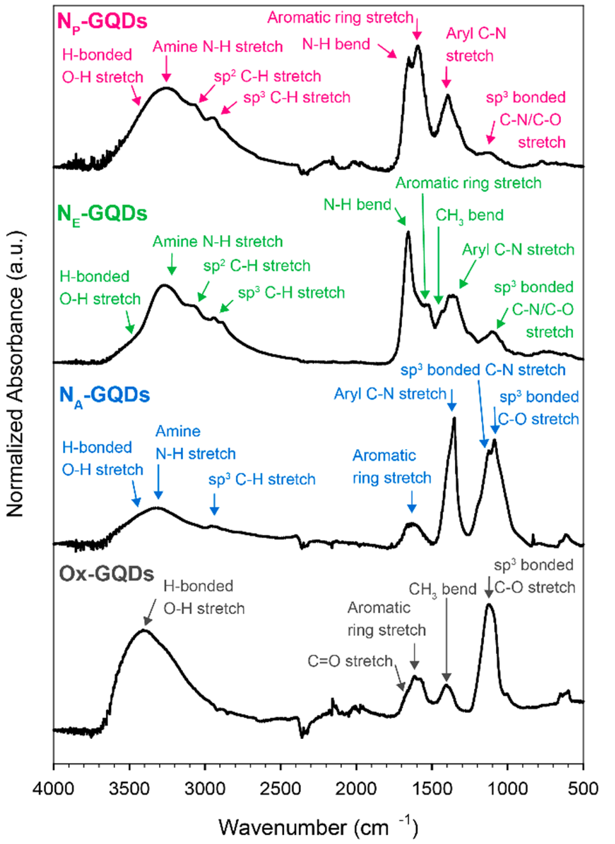

Figure 3. FT-IR spectra for the Ox-GQDs and N-GQDs produced with ammonia, ethylenediamine, and pyridine.

The functional groups of the LAL-prepared GQDs were further investigated by XPS. The XPS survey spectra are shown in Figure S3, and the resultant elemental ratios are presented in Table S2. The Ox-GQDs consist of mainly carbon (64.8%) and oxygen (33.5%). The small amount of nitrogen present is likely due to adsorbed nitrogen from the atmosphere. Among the three types of the N-GQDs, the nitrogen content increases from 4.8% in the N_A-GQDs to 10.2% in the N_p-GQDs and to 23.% in the N_E-GQDs. The highest content of nitrogen in the N_E-GQDs is consistent with the fact that each ethylenediamine molecule has two nitrogen atoms and with a previous report that primary amines allow for high degrees of nitrogen doping.[25] While all three nitrogen doped samples contain oxygen, the N_A-GQDs contain the largest fraction of oxygen (55.9%), and the N_p-GQDs have the largest fraction of carbon (68.2%) out of all of the samples. Figure 4 presents the XPS C 1s high resolution spectra for all four samples, and their binding energies and relative contributions are summarized in Table S3. The deconvoluted spectra show the presence of sp^2- and sp^3-C in the carbon domain and C−N, hydroxyl C−O, carbonyl C═O, and carboxylic O−C═O bonded carbon at 284.5, 285.3, 286.1, 287.0, 288.0, and 289.0 eV, respectively.[47−49] The Ox-GQDs are the only samples where the relative amounts of the sp^2 bonded carbons are higher than the sp^3 bonded carbons. For the Ox-GQDs, hydroxyl groups are the major functional group, with carbonyl and carboxylic groups also present. For the N-doped GQDs, the C−N bonded carbon is dominant over all oxygen containing functional groups, and the hydroxyl groups have a higher fraction than the carbonyl and carboxylic groups. The N_P-GQDs have the highest fraction of the sp^2 carbons (26.2%) out of all of the N-GQDs which is attributed to the pyridine nitrogen source maintaining its sp^2 nature during doping.

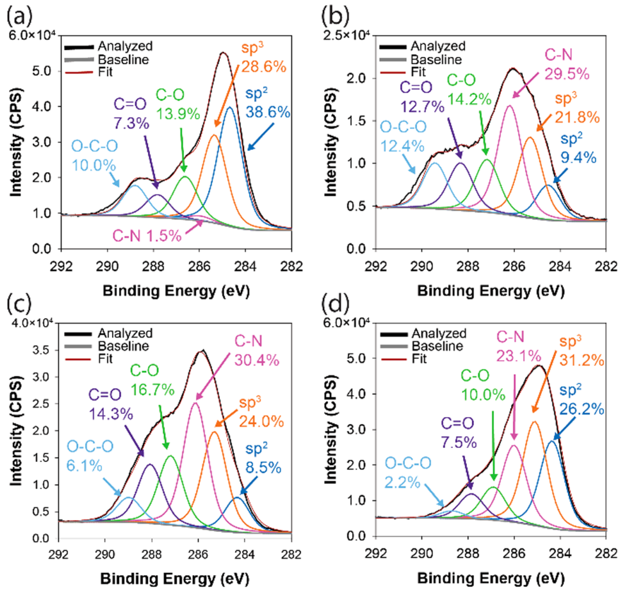

Figure 4. High resolution C 1s XPS spectra for the Ox-GQDs (a) and N-GQDs produced with ammonia (b), ethylenediamine (c), and pyridine (d).

The various nature of nitrogen doping of the N-GQDs was investigated by analyzing the N 1s XPS spectra. The N 1s XPS raw and deconvoluted spectra are presented in Figure 5a−c, and their total nitrogen content is presented in Figure 5d. The binding energies and relative contributions are summarized in Table S4. All three types of the N-GQDs have a mixture of pyridinic, amine, pyrrolic, and graphitic nitrogen at 398.8, 399.7, 400.7, and 401.8 eV, respectively.[47,50,51] Although specific types of nitrogen precursors were used for the doping, nitrogen is converted to various chemical states after incorporation. For the N_A-GQDs and N_E-GQDs, the dominant functional groups are amine and pyrrolic nitrogen with the N_A-GQDs having considerably less total nitrogen functional groups than the N_E-GQDs. The N_E-GQDs have the largest fraction of amine functional groups among the three N-GQDs which accounts for 49.3% of the nitrogen containing functional groups. Overall, nitrogen precursor solutes were found to influence both the total amount of incorporated nitrogen and the distribution of functional groups. For example, the N_E-GQDs retain the largest amount of amines, although a fraction of amines is converted to pyridinic, pyrrolic, and graphitic nitrogen. While the N_E-GQDs and N_P-GQDs both contain similar amounts of pyridinic and graphitic nitrogen, these functional groups contribute to a higher percentage of the N_P-GQDs, with the pyridinic group accounting for 31.3% and the graphitic group accounting for 13.0% of the total nitrogen sites. These results give further insight into the GQD formation mechanism. During LAL, the dopant molecules are recruited and chemically bonded to the resultant GQDs rather than just physisorbed. This is supported by the presence of various nitrogen functional groups in each N-GQD sample rather than observation of only those the functional groups present in the corresponding dopant molecule.

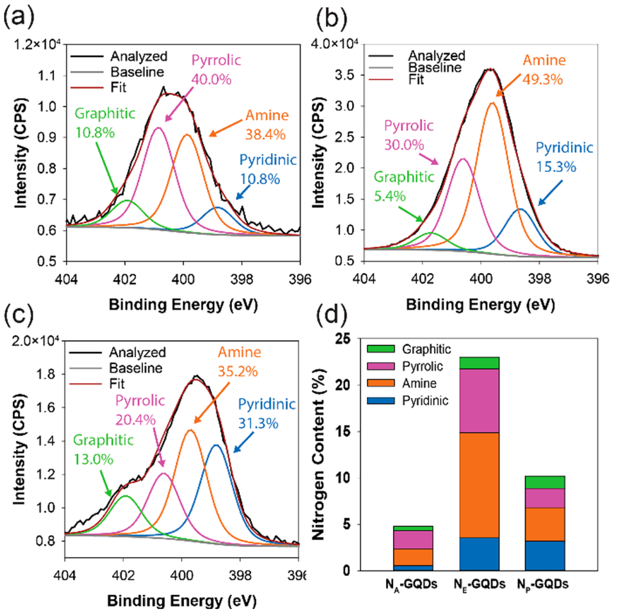

Figure 5. High resolution N 1s XPS spectra of the N-GQDs produced with ammonia (a), ethylenediamine (b), and pyridine (c). The content of each nitrogen chemical state is summarized in (d).

Figure 6a presents the UV−vis absorption spectra of the various GQD samples. The *Y* axis of the absorption spectra is extinction mass coefficient (ε, $cm^2\ g^{-1}$). For GQDs, the short wavelength absorption (<250 nm) is typically attributed to $\pi-\pi^*$ transitions of the sp^2 hybridized carbon backbone and the longer wavelength absorptions (>250 nm) are due to $n-\pi^*$ transitions of functional groups present.[52] All samples exhibit strong absorbance in the deep UV (200−210 nm) region from the $\pi-\pi^*$ transitions of the carbon backbone. None of the

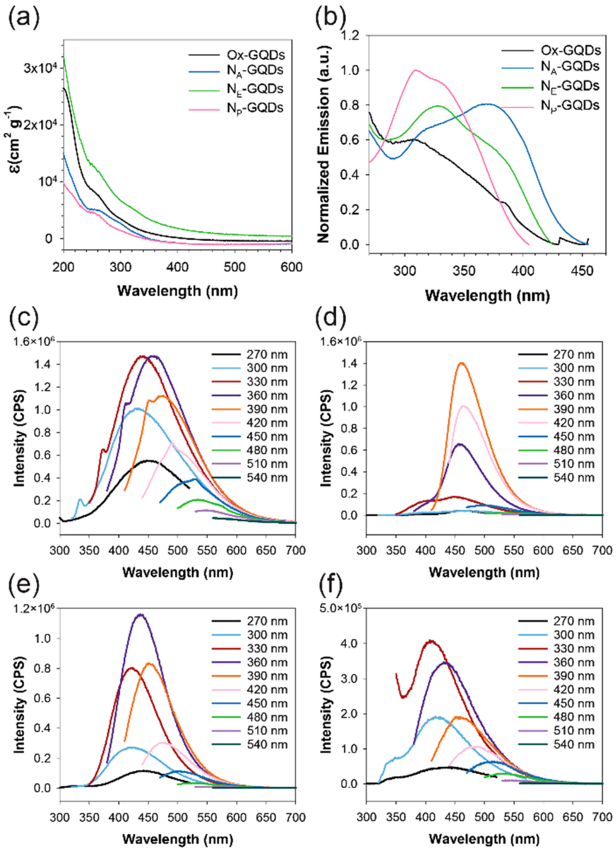

Figure 6. Absorbance spectra of the Ox-GQDs and N-GQDs produced with various precursors (a), PLE spectra collected from emissions at 445 nm for the Ox-GQDs, at 465 nm for the N$_A$-GQDs, at 435 nm for the N$_E$-GQDs, and at 415 nm for the N$_P$-GQDs (b), and PL emission spectra at various excitation wavelengths for the Ox-GQDs (c) and the N-GQDs produced with ammonia (d), ethylenediamine (e), and pyridine (f).

samples show any absorption past 450 nm which indicates that all absorbance transitions occur in the UV−blue range. As mentioned above, this also results in minimal interactions of the GQDs with the 532 nm laser pulses during LAL. The Ox-GQDs have shoulders at 265 and 350 nm which can be attributed to the n−π* transitions of various oxygenated functional groups. Similarly, the N$_A$-GQDs have a peak at 280 nm; however, it is more strongly defined. The N$_E$-GQDs have the weakest absorbance with only weakly absorbing shoulders observed at 270 and 350 nm. The N$_P$-GQDs have a shoulder occurring at 260 nm. All of the N-GQDs are only weakly absorbing in the 350−450 nm range without any well-defined features that reflect the wide distributions of surface functional groups. Figure S4 shows the absorbance and PL spectra of the precursor CNOs indicating a major change in optical properties following LAL.

The PL excitation (PLE) spectra for the various GQD samples are shown in Figure 6b. Each spectrum was collected at the emission wavelength where maximal emission occurs for each individual sample (445, 465, 435, and 415 nm for the Ox-GQDs, N$_A$-GQDs, N$_E$-GQDs, and N$_P$-GQDs, respectively). For each GQD, the profile of the PLE spectrum is quite different from its absorbance spectrum, due to the different PLQYs of the bands. For the Ox-GQDs, the strongest emission occurs with 310 nm excitation and with decreasing emission at longer wavelengths. The slight shoulder at 385 nm is due to Raman scattering of the water solvent. The N$_A$-GQDs show a gradual increase in emission with increasing excitation wavelength with a slight shoulder apparent at 325 nm and a well-defined peak at 375 nm. The N$_A$-GQDs are the only sample that has its strongest emission at a longer wavelength excitation (380 nm). The N$_E$-GQDs show peak emission with 330 nm excitation and decreasing emission at longer wavelengths and a slight shoulder at 380 nm. The N$_P$-GQDs have the shortest wavelength excitation with a peak at 310 nm and a shoulder around 330 nm. The full excitation spectra for each sample are shown in Figure S5. For the N$_A$-GQDs, two peaks at 325 and 375 nm are apparent at all emission wavelengths with the relative intensities of each peak changing with emission wavelength. At shorter emission wavelengths the peak at an excitation of 325 nm is stronger, and as the emission wavelength increases, the peak excitation shifts toward favoring 375 nm. The N$_E$-GQDs, on the other hand, show a similar excitation profile, but it shifts toward longer excitation wavelengths with increasing emission wavelength.

The PL properties were further examined by considering the emission spectra of each sample (Figure 6c−f). The Ox-GQDs have a peak emission occurring at 445 nm with 330 nm excitation. The sharp, excitation dependent shoulders on the short wavelength side of each PL curve are also due to the Raman scattering of the water solvent. The N$_A$-GQDs have peak emission occurring at 465 nm with 390 nm excitation. At 330 nm excitation, a shoulder is also observed at 400 nm emission but is suppressed at excitation wavelengths longer than 360 nm. The N$_E$-GQDs have the strongest emission occurring at 435 nm with 360 nm excitation, and the N$_P$-GQDs peak emission occurs at 415 nm with 330−360 nm excitation. It is observed that all four GQDs exhibit some combination of both excitation independent and excitation dependent emission. For the Ox-, N$_E$-, and N$_p$-GQDs, the excitation independent emission is observed at shorter wavelengths and excitation dependent emission is observed at longer excitation wavelength. For the N$_A$-GQDs, the excitation dependence is only weakly observed while excitation independent emission is strongly observed at 465 nm emission. The excitation dependent emission is attributed to nonuniform sp^2 carbon domains within a sample favoring different emissions based on the quantum confinement effect. These emissions are weaker than the excitation independent emissions that are attributed to emission from functional groups.[13,53]

The emissive properties can be understood by considering the functional groups present in the samples. The Ox-GQDs have the weakest emission out of all the samples, which is expected since they lack nitrogen doping that is expected to enhance the emission. The peak emission at 445 nm is attributed to emission from the large fraction of hydroxyl groups as carboxyl groups are expected to contribute to longer wavelength emissions.[16] It has been reported that amine and pyrrolic nitrogens red-shift emission while edge pyridinic nitrogen blue-shifts the emission.[54] The N$_A$-GQDs have amine nitrogen as their primary nitrogen functional group, and we assign the strong excitation independent emission at 465 nm to be from these amine groups. The N$_E$-GQDs have a high nitrogen content; while they favor amine and pyrrolic nitrogen, they still have a high number of pyridinic and graphitic nitrogen sites. This results in strong excitation dependent emission from the various types of nitrogen doping. The bluer emission occurs due to the pyridinic nitrogen, and redder emission is mainly from the amine nitrogen. The N_P-GQDs have the bluest emission among all GQDs, attributable to the largest fraction of the pyridinic nitrogen. They also have the largest fraction of the graphitic nitrogen, and while it is reported that the graphitic nitrogen can red-shift emission,[19] we expect this to have minimal effect due to the large fraction of the sp^3 carbon causing disordered structures and small sp^2 carbon domain sizes. On the basis of these observations, we can assign the PLE bands observed in the N-GQDs. The N_P-GQDs have the strongest emission with shorter wavelength excitation (310 nm) which is mainly influenced by transitions related to the pyridinic nitrogen. The N_A-GQDs exhibit the strongest emission at longer wavelength excitation (380 nm) due to mainly amine nitrogen groups. N_E-GQDs have a large number of both types of nitrogen and demonstrate strong bands at both wavelengths.

Fluorescence intensity decay measurements were performed at 390 nm excitation and measured at 425 (Figure 7a) and 465 nm emission (Figure 7b.) The fluorescence intensity decay profile tracks the deactivation kinetics of electrons from an excited state to the ground state via radiative and nonradiative paths. The decay curves were fit to three exponentials as is common with previously reported measurements.[15] The lifetimes and their overall contributions are summarized in Table 1, and the complete fit parameters are shown in Tables S4 and S5. All decays had a fast component (τ_1) from the radiative recombination of the intrinsic states[13] and two slower components (τ_2 and τ_3) that are attributed to the surface functional groups.[15]

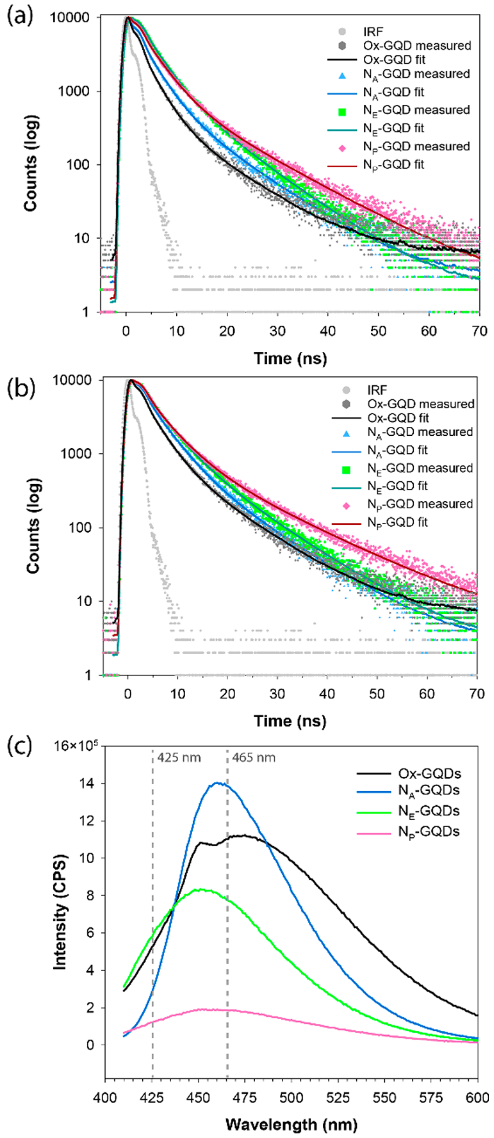

Figure 7. TCSPC of the Ox-GQDs and N-GQDs and the corresponding IRF at 425 nm (a) and 465 nm (b) emission. PL spectra at 393 nm excitation (c).

We previously reported that for GQDs containing a mixture of hydroxyl and carboxylic groups the intrinsic state showed the fluorescence decay with the fast τ_1 component and was weakly emitting, while the hydroxyl groups were responsible for the intermediate τ_2 component and carboxylic groups were responsible for the longest τ_3 component, and both functional groups were strongly emitting.[32] Other reports also suggest that the intrinsic states have low PLQYs with a fast nonradiative deactivation component.[13] It also has been suggested that functional groups with a higher degree of oxidation or polarity will have a longer lifetime component that also increases with increasing emission wavelength.[55]

Here, we observe a similar trend for the current GQD samples. The τ_1 component is slower at 465 nm emission than at 425 nm emission. Since the τ_1 is related to the intrinsic states from the sp^2 carbon domains, the shift to longer wavelengths relates to the emission from larger carbon domains that have a smaller energy gap. The relative contributions also change due to varying amounts of the different sized sp^2 carbon domains. Out of the three different decays, the τ_1 is the least similar when comparing the various samples, which can be explained by the large amount of the disorder and sp^3 carbon within the samples. With 390 nm excitation, the emission intensity for the Ox-GQDs is significantly higher at 465 nm than at 425 nm (Figure 7c.). The relative contributions of the τ_2 and τ_3 components also increase at 465 nm emission, which further supports that these decays are due to components with a strong radiative nature. Since the Ox-GQDs only have oxygen containing functional groups, we assign the τ_2 to hydroxyl groups and the τ_3 to more oxidized and polar carboxylic groups similar to previous work.[32,55] Since hydroxyl groups account for the highest percentage of oxygen containing functional groups on the Ox-GQDs, it makes sense that the τ_2 component will have the highest relative contribution.

The N_A-GQDs also show a significant increase in emission intensity with the shift from 425 to 465 nm emission. While τ_2 shows a higher relative contribution at 465 nm, the τ_3 component does not show any significant difference between the two emissions. The dominant functional groups on the N_A-GQDs are hydroxyl and amine groups, so we expect them to be the major contributing factors in the τ_2 decay. While the intrinsic τ_1 component is present at 465 nm emission, it is expected to have a low PLQY and minimally contribute to the emission.[32] Therefore, the strong emission observed at 465 nm is assigned to surface functional groups from the τ_2 component. Both the N_E-GQDs and N_P-GQDs show only a slight increase in emission intensity at 465 nm, and their τ_2 and τ_3 components have much less difference at the two emission wavelengths. For both samples, the τ_2 component decreases slightly, while the τ_3 component increases slightly. The emission peaks at 390 nm excitation are also blue-shifted relative to the Ox-GQDs and N_A-GQDs. As previously

Table 1. Time Correlated Single Photon Counting Lifetimes and Relative Contributions of the Ox-GQDs and N-GQDs at 425 and 465 nm Emission

	Ox-GQDs		N_A-GQDs		N_E-GQDs		N_P-GQDs	
	lifetime (ns)	contribution (%)	lifetime (ns)	contribution (%)	lifetime (ns)	contribution (%)	lifetime (ns)	contribution (%)
				λ_{em} = 425 nm				
τ_1	0.346(10)	39.0(8)	0.355(12)	28.6(7)	0.92(5)	16.5(8)	0.56(3)	19.4(8)
τ_2	2.71(5)	44.0(7)	3.02(5)	48.9(6)	3.52(4)	56.5(6)	3.56(3)	55.0(6)
τ_3	9.13(8)	17.0(3)	9.17(6)	22.5(3)	8.86(5)	27.0(3)	11.43(5)	25.6(3)
				λ_{em} = 465 nm				
τ_1	0.60(2)	24.0(5)	0.80(3)	20.0(6)	1.09(2)	18.2(4)	1.15(2)	19.2(4)
τ_2	3.24(6)	51.7(6)	3.92(4)	57.3(4)	4.17(11)	53.2(7)	4.44(9)	53.5(5)
τ_3	9.58(7)	24.3(3)	10.01(7)	22.7(3)	9.91(6)	28.6(4)	13.31(7)	27.3(3)

mentioned, the N_E-GQDs have a high nitrogen content which contributes to excitation dependent emission and a high quantity of different types of emitting functional groups. Since the τ_2 component is attributed to amine functional groups, we expect τ_3 to be strongly influenced by the more polar, pyridinic nitrogen sites. Finally, it is noted that the τ_3 component for the N_P-GQDs is noticeably slower when compared to the other samples. The N_P-GQDs have the highest overall percentage of pyridinic nitrogen and the bluest shifted emission out of all of the samples. If the τ_3 component is influenced by the pyridinic nitrogen groups, it makes sense that the N_P-GQDs would have such a long lifetime at 390 nm excitation because the radiative component of deactivations is quite weak as shown by the weak emission at 390 nm excitation in the PLE spectra regardless of the emission wavelength (Figure S5d). The emission at 465 nm could be due to an energy transfer process because it would take longer for the higher energy states of the N_P-GQDs to decay to longer wavelengths before emitting. Since the N_P-GQDs are only weakly emitting with 390 nm excitation, we expect τ_3 for this sample to have a strong nonradiative component and a weak radiative component.

The PLQY of the GQDs was measured relative to a quinine sulfate standard (Figures S6−S8). The Ox-GQDs had a PLQY of 0.81(7)%. The addition of nitrogen resulted in an increase of PLQY with N_A-, N_E-, and N_P-GQDs having PLQYs of 3.8(5)%, 8.6(4)%, and 4.6(3)%, respectively. Total nitrogen content clearly influenced the PLQY as N_E-GQDs had both the highest nitrogen content and the highest PLQY while N_A-GQDs had both the lowest nitrogen content and PLQY of the three N-GQDs. The photostability of the GQDs was considered by measuring their emission at continuous excitation for 1 h at their maximum excitation and emission wavelengths (Figure S9). All four samples showed a decrease in intensity of less than 7%, indicating the samples are stable in water under continuous excitation and suitable for applications that use similar conditions of excitation intensity. Finally, the effects additional purification had on the spectra were considered. Samples were dialyzed for 1 week in a 1000 Da molecular weight cutoff membrane to remove any small side products that could have formed during LAL. Spectra were collected both before and after dialysis (Figure S10a−h) and showed very similar PL profiles, which indicates that the emitting species is retained in the dialysis membrane. The outer solution was also analyzed (Figure S10i−l) and only showed minimal emission. These results support LAL as a method to produce PL materials in a way that is fast and requires minimal purification.

To test the catalytic performance of the N-GQDs for the ORR reaction, CV curves were recorded in either N_2 saturated or O_2 saturated electrolyte. The performance of the N-GQDs was compared to those of Pt/C and carbon black support in the absence of the GQDs (Figure S11). Each CV curve was corrected for *IR* (current times resistance) to compensate for a large resistance that is due to the large content of nafion (Table S12). All samples showed featureless CV curves in the N_2 saturated environment, indicating that no faradaic reactions are taking place. For all samples in an O_2 saturated environment, as the potential was swept toward a more negative voltage, a clear increase in reduction current density is apparent due to the occurrence of the ORR reaction.

RDE measurements and their Koutecky−Levich plots are reported in Figure 8a−d for the GQD samples and in Figure S12 for the reference samples. A plot of the calculated electron transfer numbers is shown in Figure 8e, and an overlay of RDE LSV scans for each sample at 1600 rpm is shown in Figure 8f. RDE measurements were performed at rotation speeds ranging from 400 to 3200 rpm, and potentials ranging from 0.46 to −0.24 V (vs RHE) were analyzed to determine electron transfer numbers. Details of the Koutecky−Levich equation are included in the Supporting Information. For Pt/C the electron transfer number is close to 4 at low potentials but decreases slightly at higher potentials indicating slight peroxide formation. The Ox-GQDs show an electron transfer number slightly lower than 2 which could indicate a mix of a two-electron pathway to form peroxide and one-electron pathway to form superoxide.[56] The N_E-GQDs have an electron transfer number close to 3 at low applied potentials that approaches 2 as the potential becomes more negative. The N_A-GQDs, N_P-GQDs, and carbon black all show an electron transfer number that favors a two-electron process at all potentials, indicating good selectivity for peroxide formation. All LSV scans were swept from 1.26 to −0.24 V (vs RHE). Compared to the onset potential of carbon black (0.70 V), all GQD samples showed positively shifted onset potentials (N_A-GQDs, 0.72 V; N_E-GQDs, 0.74 V; N_P-GQDs, 0.75 V). It has been reported that carbon atoms neighboring pyridinic sites have the best catalytic activity,[57] so it is not surprising that the N_E-GQDs and N_P-GQDs show the lowest onset potentials as they contain a comparable number of pyridinic and graphitic sites. Moreover, the N_E-GQDs and N_P-GQDs have shown the largest ORR current densities among the GQD samples, exceeding the N_A-GQDs, Ox-GQDs, and carbon black (Figure 8f). The Pt/C reference sample had the lowest onset potential at 0.90 V and the highest current density out of all of the samples; however, it should be noted that this reference is catalyzing a four-electron primarily over the two-electron process which was favored by all of the carbon samples. It is also apparent that for most RDE and RRDE measurements two separate increases in

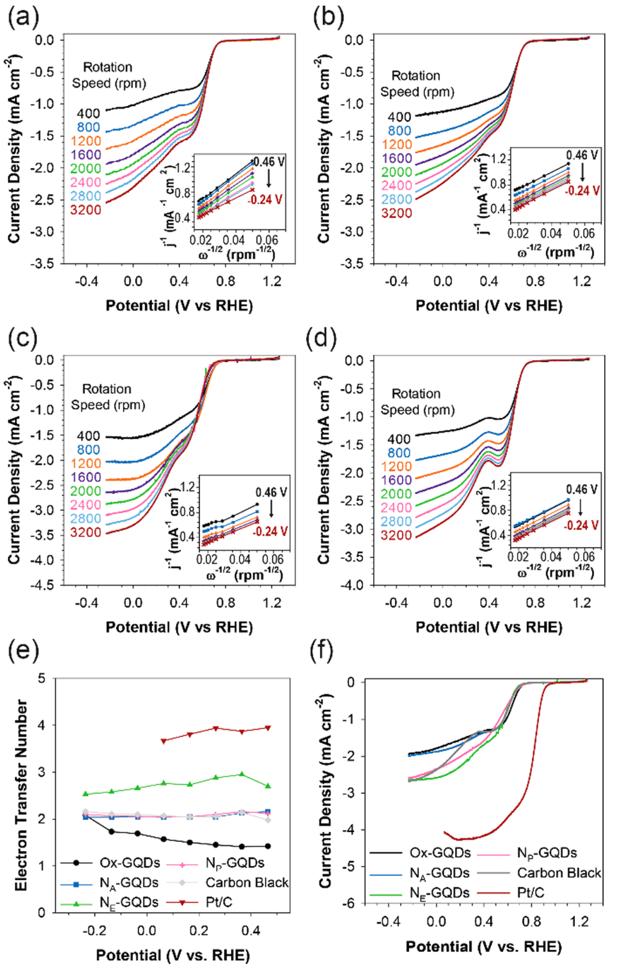

Figure 8. RDE LSV scans for the Ox-GQDs (a), Na-GQDs (b), Ne-GQDs (c), and Np-GQDs (d) and their derived KL plots (insets). For the insets the various potentials are represented by black circles at −0.5 V, blue squares at −0.6 V, orange triangles at −0.7 V, purple crosses at −0.8 V, green hexes at −0.9 V, pink diamonds at −1.0 V, light blue inverted triangles at −1.1 V, and red crosses at −1.2 V. Electron transfer numbers (e, and overlaid LSV scans of each sample collected at 1600 rpm (f).

current density are observed. This is especially prominent in the N_P-GQDs. We attribute the feature of two increasing currents to the disturbance of mass transfer due to the porous nature of the samples during the rotations of electrodes, not to the presence of multiple catalytic sites.

RRDE measurements are reported in Figure 9a−d for the GQD samples and Figure S13 for the reference samples. In Figure 9a−d, the disk current is from ORR occurring at each GQD working electrode while the ring current is from oxidation of hydrogen peroxide produced from ORR. From the RRDE results, electron transfer numbers are determined for each GQD. The plots of the determined electron transfer number and the percentage of hydrogen peroxide produced are shown in Figure 9e,f. Similar to the RDE measurements, the RRDE shows that all three N-GQD samples have an electron transfer number close to 2 consistently across all applied potentials. Their percent hydrogen peroxide production is close to 80% which indicates good selectivity toward the two-electron process. The Ox-GQDs have much lower selectivity at 60% which decreases with increased applied potential. It should be noted that the electron transfer numbers for the Ox-GQDs calculated by RRDE are significantly different from the RDE measurements. For the Ox-GQDs, not only ORR but also the reduction of oxygen-containing functional groups present in the sample contribute to the overall reduction current, as is previously reported.[58] Therefore, electrochemical measurements alone without separate product analyses are less reliable for the determination of ORR pathway for Ox-GQDs. The N-GQDs presented better consistency. Due to their low onset potentials and high selectivity toward the two-electron process, both N_E-GQDs and N_P-GQDs are good candidates for electrocatalysis of hydrogen peroxide formation. Due to the high resistance of the electrodes, further work could improve this process by increasing the hydrophobicity of the GQDs so that they require a lower Nafion content as a binder.

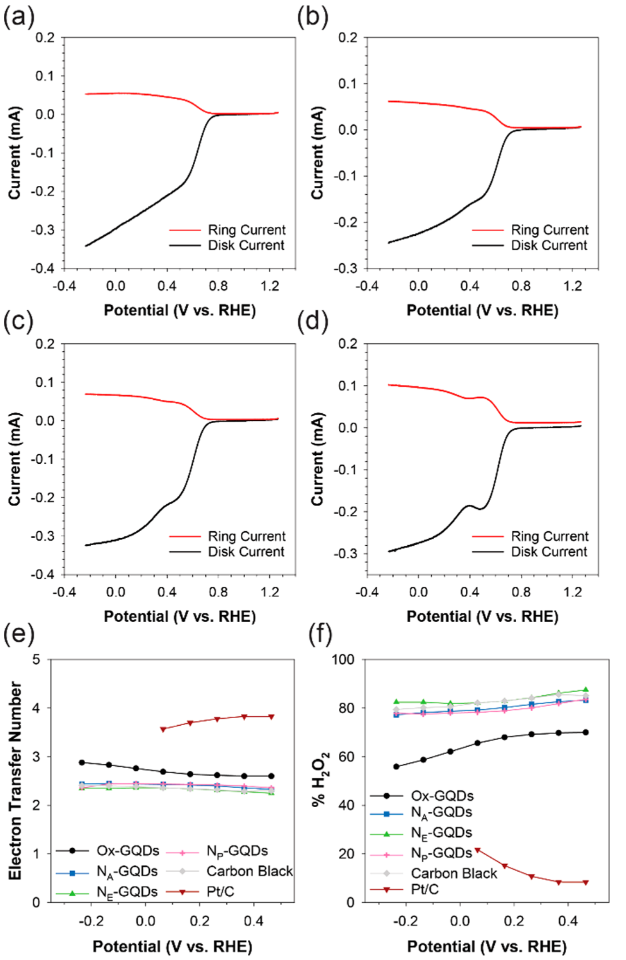

Figure 9. RRDE LSV scans for the Ox-GQDs (a), Na-GQDs (b), Ne-GQDs (c), and Np-GQDs (d). Electron transfer numbers (e) and % H_2O_2 formation (f) for the Ox-GQDs (black circles), Na-GQDs (blue squares), Ne-GQDs (green triangles), carbon black only (gray diamonds), and Pt/C (red inverted triangles).

In conclusion, we have prepared nitrogen doped GQDs from CNOs using laser ablation in liquid. This method offered several advantages over traditional methods due to few byproducts, fast production times, and the tunability of the PL and functional groups. The choice of solutes in the liquid allowed for tuning of the types of nitrogen functional groups that were present and also influenced the overall nitrogen content. The resultant N-GQDs had PL properties that were tunable based on the ratios of N-functional groups. It was observed that a high content of amine functional groups resulted in more red-shifted emission, while a high concentration of pyridinic nitrogen significantly blue-shifted the emission. PL lifetime measurements indicated that intrinsic states have a fast decay, while the functional groups exist as extrinsic states with slower decays. A combination of hydroxyl and amine functional groups leads to a decay in the 3−4 ns range, while the more polar carboxylic or pyridinic groups have decays that range from 9 to 13 ns. These N-GQDs exhibited highly selective catalytic activity toward the two-electron process for the ORR, with the N_E-GQDs and N_P-GQDs having the best onset potentials and selectivity. Future works will look toward improving the catalytic performance by increasing the hydrophobicity of the samples through tuning of laser solution parameters, and alternative, more readily available carbon precursors will also be explored. Finally, it should be noted that the choice of solvent and its properties such as polarity and viscosity may significantly influence PL lifetime and PLQY of GQDs and should be considered for applications.

■ ASSOCIATED CONTENT

Supporting Information

The Supporting Information is available free of charge on the ACS Publications website at DOI: 10.1021/acsanm.9b01433.

> Particle diameter and height distributions, XPS survey scans and high-resolution fit details, optical data of CNOs, excitation spectra at various emission wavelength, TCSPC details, determined PLQYs, photostability results, purification effects, and electrochemical measurement details and data for reference scans (PDF)

■ AUTHOR INFORMATION

Corresponding Authors

*D.-S.Y.: e-mail, dyang0@uky.edu.
*D.Y.K.: e-mail, dooyoung.kim@uky.edu.

ORCID

Rosemary L. Calabro: 0000-0001-9394-5385
Dong-Sheng Yang: 0000-0001-9842-4343
Doo Young Kim: 0000-0002-6095-5023

Author Contributions

All authors have given approval to the final version of the manuscript.

Notes

The authors declare no competing financial interest.

■ ACKNOWLEDGMENTS

We acknowledge financial support from the National Science Foundation under Cooperative Agreement 1355438 (D.Y.K.) and Kentucky Science & Engineering Foundation Grant KSEF-3884-RDE-020 (D.Y.K.), the National Science Foundation Division of Chemistry (Grant 1800316, D.S.Y.), and the University of Kentucky Research Challenge Trust Fund (R.L.C.).

■ REFERENCES

(1) Sun, H.; Wu, L.; Wei, W.; Qu, X. Recent Advances in Graphene Quantum Dots for Sensing. *Mater. Today* **2013**, *16* (11), 433−442.

(2) Qian, Z. S.; Shan, X. Y.; Chai, L. J.; Ma, J. J.; Chen, J. R.; Feng, H. A Universal Fluorescence Sensing Strategy Based on Biocompatible Graphene Quantum Dots and Graphene Oxide for the Detection of DNA. *Nanoscale* **2014**, *6* (11), 5671−5674.

(3) Yang, W.; Zhang, H.; Lai, J.; Peng, X.; Hu, Y.; Gu, W.; Ye, L. Carbon Dots with Red-Shifted Photoluminescence by Fluorine Doping for Optical Bio-Imaging. *Carbon* **2018**, *128*, 78−85.

(4) Cui, B.; Feng, X.-t.; Zhang, F.; Wang, Y.-l.; Liu, X.-g.; Yang, Y.-z.; Jia, H.-s. The Use of Carbon Quantum Dots as Fluorescent Materials in White Leds. *New Carbon Materials* **2017**, *32* (5), 385−401.

(5) Markovic, Z. M.; Ristic, B. Z.; Arsikin, K. M.; Klisic, D. G.; Harhaji-Trajkovic, L. M.; Todorovic-Markovic, B. M.; Kepic, D. P.; Kravic-Stevovic, T. K.; Jovanovic, S. P.; Milenkovic, M. M.; Milivojevic, D. D.; Bumbasirevic, V. Z.; Dramicanin, M. D.; Trajkovic, V. S. Graphene Quantum Dots as Autophagy-Inducing Photodynamic Agents. *Biomaterials* **2012**, *33* (29), 7084−7092.

(6) Jovanović, S. P.; Syrgiannis, Z.; Marković, Z. M.; Bonasera, A.; Kepić, D. P.; Budimir, M. D.; Milivojević, D. D.; Spasojević, V. D.; Dramićanin, M. D.; Pavlović, V. B.; Todorović Marković, B. M. Modification of Structural and Luminescence Properties of Graphene Quantum Dots by Gamma Irradiation and Their Application in a Photodynamic Therapy. *ACS Appl. Mater. Interfaces* **2015**, *7* (46), 25865−25874.

(7) Zou, X.; Liu, M.; Wu, J.; Ajayan, P. M.; Li, J.; Liu, B.; Yakobson, B. I. How Nitrogen-Doped Graphene Quantum Dots Catalyze Electroreduction of Co2 to Hydrocarbons and Oxygenates. *ACS Catal.* **2017**, *7* (9), 6245−6250.

(8) Fernando, K. A. S.; Sahu, S.; Liu, Y.; Lewis, W. K.; Guliants, E. A.; Jafariyan, A.; Wang, P.; Bunker, C. E.; Sun, Y.-P. Carbon Quantum Dots and Applications in Photocatalytic Energy Conversion. *ACS Appl. Mater. Interfaces* **2015**, *7* (16), 8363−8376.

(9) Li, Q.; Zhang, S.; Dai, L.; Li, L.-s. Nitrogen-Doped Colloidal Graphene Quantum Dots and Their Size-Dependent Electrocatalytic Activity for the Oxygen Reduction Reaction. *J. Am. Chem. Soc.* **2012**, *134* (46), 18932−18935.

(10) Bacon, M.; Bradley, S. J.; Nann, T. Graphene Quantum Dots. *Part. Part. Syst. Charact.* **2014**, *31* (4), 415−428.

(11) Li, L.; Wu, G.; Yang, G.; Peng, J.; Zhao, J.; Zhu, J.-J. Focusing on Luminescent Graphene Quantum Dots: Current Status and Future Perspectives. *Nanoscale* **2013**, *5* (10), 4015−4039.

(12) Zhao, M.; Yang, F.; Xue, Y.; Xiao, D.; Guo, Y. A Time-Dependent Dft Study of the Absorption and Fluorescence Properties of Graphene Quantum Dots. *ChemPhysChem* **2014**, *15* (5), 950−957.

(13) Wang, L.; Zhu, S.-J.; Wang, H.-Y.; Wang, Y.-F.; Hao, Y.-W.; Zhang, J.-H.; Chen, Q.-D.; Zhang, Y.-L.; Han, W.; Yang, B.; Sun, H.-B. Unraveling Bright Molecule-Like State and Dark Intrinsic State in Green-Fluorescence Graphene Quantum Dots Via Ultrafast Spectroscopy. *Adv. Opt. Mater.* **2013**, *1* (3), 264−271.

(14) Wang, S.; Cole, I. S.; Zhao, D.; Li, Q. The Dual Roles of Functional Groups in the Photoluminescence of Graphene Quantum Dots. *Nanoscale* **2016**, *8* (14), 7449−7458.

(15) Bao, L.; Zhang, Z.-L.; Tian, Z.-Q.; Zhang, L.; Liu, C.; Lin, Y.; Qi, B.; Pang, D.-W. Electrochemical Tuning of Luminescent Carbon Nanodots: From Preparation to Luminescence Mechanism. *Adv. Mater.* **2011**, *23* (48), 5801−5806.

(16) Zhu, S.; Shao, J.; Song, Y.; Zhao, X.; Du, J.; Wang, L.; Wang, H.; Zhang, K.; Zhang, J.; Yang, B. Investigating the Surface State of Graphene Quantum Dots. *Nanoscale* **2015**, *7* (17), 7927−7933.

(17) Zheng, H.; Wang, Q.; Long, Y.; Zhang, H.; Huang, X.; Zhu, R. Enhancing the Luminescence of Carbon Dots with a Reduction Pathway. *Chem. Commun.* **2011**, *47* (38), 10650−10652.

(18) Permatasari, F. A.; Aimon, A. H.; Iskandar, F.; Ogi, T.; Okuyama, K. Role of C−N Configurations in the Photoluminescence of Graphene Quantum Dots Synthesized by a Hydrothermal Route. *Sci. Rep.* **2016**, *6*, 21042.

(19) Holá, K.; Sudolská, M.; Kalytchuk, S.; Nachtigallová, D.; Rogach, A. L.; Otyepka, M.; Zbořil, R. Graphitic Nitrogen Triggers Red Fluorescence in Carbon Dots. *ACS Nano* **2017**, *11* (12), 12402−12410.

(20) Sarkar, S.; Sudolská, M.; Dubecký, M.; Reckmeier, C. J.; Rogach, A. L.; Zbořil, R.; Otyepka, M. Graphitic Nitrogen Doping in Carbon Dots Causes Red-Shifted Absorption. *J. Phys. Chem. C* **2016**, *120* (2), 1303−1308.

(21) Wang, K.; Dong, J.; Sun, L.; Chen, H.; Wang, Y.; Wang, C.; Dong, L. Effects of Elemental Doping on the Photoluminescence Properties of Graphene Quantum Dots. *RSC Adv.* **2016**, *6* (94), 91225−91232.

(22) Schneider, J.; Reckmeier, C. J.; Xiong, Y.; von Seckendorff, M.; Susha, A. S.; Kasák, P.; Rogach, A. L. Molecular Fluorescence in Citric Acid-Based Carbon Dots. *J. Phys. Chem. C* **2017**, *121* (3), 2014−2022.

(23) Li, Y.; Zhao, Y.; Cheng, H.; Hu, Y.; Shi, G.; Dai, L.; Qu, L. Nitrogen-Doped Graphene Quantum Dots with Oxygen-Rich Functional Groups. *J. Am. Chem. Soc.* **2012**, *134* (1), 15−18.

(24) Tetsuka, H.; Asahi, R.; Nagoya, A.; Okamoto, K.; Tajima, I.; Ohta, R.; Okamoto, A. Optically Tunable Amino-Functionalized Graphene Quantum Dots. *Adv. Mater.* **2012**, *24* (39), 5333−5338.

(25) Qu, D.; Zheng, M.; Zhang, L.; Zhao, H.; Xie, Z.; Jing, X.; Haddad, R. E.; Fan, H.; Sun, Z. Formation Mechanism and Optimization of Highly Luminescent N-Doped Graphene Quantum Dots. *Sci. Rep.* **2015**, *4*, 5294.

(26) Wang, W.; Wang, Z.; Liu, J.; Peng, Y.; Yu, X.; Wang, W.; Zhang, Z.; Sun, L. One-Pot Facile Synthesis of Graphene Quantum Dots from Rice Husks for Fe3+ Sensing. *Ind. Eng. Chem. Res.* **2018**, *57* (28), 9144−9150.

(27) Wang, G.; Guo, Q.; Chen, D.; Liu, Z.; Zheng, X.; Xu, A.; Yang, S.; Ding, G. Facile and Highly Effective Synthesis of Controllable Lattice Sulfur-Doped Graphene Quantum Dots Via Hydrothermal Treatment of Durian. *ACS Appl. Mater. Interfaces* **2018**, *10* (6), 5750−5759.

(28) Lin, T. N.; Chih, K. H.; Yuan, C. T.; Shen, J. L.; Lin, C. A. J.; Liu, W. R. Laser-Ablation Production of Graphene Oxide Nanostructures: From Ribbons to Quantum Dots. *Nanoscale* **2015**, *7* (6), 2708−2715.

(29) Russo, P.; Hu, A.; Compagnini, G.; Duley, W. W.; Zhou, N. Y. Femtosecond Laser Ablation of Highly Oriented Pyrolytic Graphite: A Green Route for Large-Scale Production of Porous Graphene and Graphene Quantum Dots. *Nanoscale* **2014**, *6* (4), 2381−2389.

(30) Gokhale, R. R.; Thakare, V. P.; Warule, S.; Lefez, B.; Hannoyer, B.; Jog, J. P.; Ogale, S. B. From Small Aromatic Molecules to Functional Nanostructured Carbon by Pulsed Laser-Induced Photochemical Stitching. *AIP Adv.* **2012**, *2* (2), 022130.

(31) Castro, H. P. S.; Souza, V. S.; Scholten, J. D.; Dias, J. H.; Fernandes, J. A.; Rodembusch, F. S.; dos Reis, R.; Dupont, J.; Teixeira, S. R.; Correia, R. R. B. Synthesis and Characterisation of Fluorescent Carbon Nanodots Produced in Ionic Liquids by Laser Ablation. *Chem. - Eur. J.* **2016**, *22* (1), 138−143.

(32) Calabro, R. L.; Yang, D.-S.; Kim, D. Y. Liquid-Phase Laser Ablation Synthesis of Graphene Quantum Dots from Carbon Nano-Onions: Comparison with Chemical Oxidation. *J. Colloid Interface Sci.* **2018**, *527*, 132−140.

(33) Zeng, H.; Du, X.-W.; Singh, S. C.; Kulinich, S. A.; Yang, S.; He, J.; Cai, W. Nanomaterials Via Laser Ablation/Irradiation in Liquid: A Review. *Adv. Funct. Mater.* **2012**, *22* (7), 1333−1353.

(34) Zuo, P.; Lu, X.; Sun, Z.; Guo, Y.; He, H. A Review on Syntheses, Properties, Characterization and Bioanalytical Applications of Fluorescent Carbon Dots. *Microchim. Acta* **2016**, *183* (2), 519−542.

(35) Sajti, C. L.; Sattari, R.; Chichkov, B. N.; Barcikowski, S. Gram Scale Synthesis of Pure Ceramic Nanoparticles by Laser Ablation in Liquid. *J. Phys. Chem. C* **2010**, *114* (6), 2421−2427.

(36) Amendola, V.; Meneghetti, M. What Controls the Composition and the Structure of Nanomaterials Generated by Laser Ablation in Liquid Solution? *Phys. Chem. Chem. Phys.* **2013**, *15* (9), 3027−3046.

(37) Zhang, D.; Gökce, B.; Barcikowski, S. Laser Synthesis and Processing of Colloids: Fundamentals and Applications. *Chem. Rev.* **2017**, *117* (5), 3990−4103.

(38) Novodchuk, I.; Irannejad, M.; Wales, B.; Ibrahim, K.; Sanderson, J.; Bajcsy, M.; Yavuz, M. Controlled Volume Production of Simultaneously B/N Co-Doped Reduced Graphene Oxide Nanoflakes Using Femtosecond Laser Ablation. *Mater. Res. Bull.* **2019**, *111*, 80−86.

(39) Santiago, S. R. M.; Lin, T. N.; Chang, C. H.; Wong, Y. A.; Lin, C. A. J.; Yuan, C. T.; Shen, J. L. Synthesis of N-Doped Graphene Quantum Dots by Pulsed Laser Ablation with Diethylenetriamine (Deta) and Their Photoluminescence. *Phys. Chem. Chem. Phys.* **2017**, *19* (33), 22395−22400.

(40) Xu, H.; Yan, L.; Nguyen, V.; Yu, Y.; Xu, Y. One-Step Synthesis of Nitrogen-Doped Carbon Nanodots for Ratiometric Ph Sensing by Femtosecond Laser Ablation Method. *Appl. Surf. Sci.* **2017**, *414*, 238−243.

(41) Santiago, S. R. M.; Wong, Y. A.; Lin, T. N.; Chang, C. H.; Yuan, C. T.; Shen, J. L. Effect of Nitrogen Doping on the Photoluminescence Intensity of Graphene Quantum Dots. *Opt. Lett.* **2017**, *42* (18), 3642−3645.

(42) Gong, K.; Du, F.; Xia, Z.; Durstock, M.; Dai, L. Nitrogen-Doped Carbon Nanotube Arrays with High Electrocatalytic Activity for Oxygen Reduction. *Science* **2009**, *323* (5915), 760−764.

(43) Yang, S.; Verdaguer-Casadevall, A.; Arnarson, L.; Silvioli, L.; Čolić, V.; Frydendal, R.; Rossmeisl, J.; Chorkendorff, I.; Stephens, I. E. L. Toward the Decentralized Electrochemical Production of H2o2: A Focus on the Catalysis. *ACS Catal.* **2018**, *8* (5), 4064−4081.

(44) Choi, C. H.; Kwon, H. C.; Yook, S.; Shin, H.; Kim, H.; Choi, M. Hydrogen Peroxide Synthesis Via Enhanced Two-Electron Oxygen Reduction Pathway on Carbon-Coated Pt Surface. *J. Phys. Chem. C* **2014**, *118* (51), 30063−30070.

(45) Kim, H. W.; Ross, M. B.; Kornienko, N.; Zhang, L.; Guo, J.; Yang, P.; McCloskey, B. D. Efficient Hydrogen Peroxide Generation Using Reduced Graphene Oxide-Based Oxygen Reduction Electrocatalysts. *Nature Catalysis* **2018**, *1* (4), 282−290.

(46) Pavia, D. L.; Lampman, G. M.; Kriz, G. S.; Vyvyan, J. R. *Introduction to Spectroscopy*, 4th ed.; Brooks/Cole, Cengage Learning: Belmont, CA, 2009; pp xv, 656, 648, 658, 615.

(47) Lin, L.; Song, X.; Chen, Y.; Rong, M.; Zhao, T.; Jiang, Y.; Wang, Y.; Chen, X. One-Pot Synthesis of Highly Greenish-Yellow Fluorescent Nitrogen-Doped Graphene Quantum Dots for Pyrophosphate Sensing Via Competitive Coordination with Eu3+ Ions. *Nanoscale* **2015**, *7* (37), 15427−15433.

(48) Chua, C. K.; Sofer, Z.; Šimek, P.; Jankovský, O.; Klímová, K.; Bakardjieva, S.; Hrdličková Kučková, Š.; Pumera, M. Synthesis of Strongly Fluorescent Graphene Quantum Dots by Cage-Opening Buckminsterfullerene. *ACS Nano* **2015**, *9* (3), 2548−2555.

(49) Chua, C. K.; Pumera, M. Selective Removal of Hydroxyl Groups from Graphene Oxide. *Chem. - Eur. J.* **2013**, *19* (6), 2005−2011.

(50) Tang, L.; Ji, R.; Li, X.; Teng, K. S.; Lau, S. P. Energy-Level Structure of Nitrogen-Doped Graphene Quantum Dots. *J. Mater. Chem. C* **2013**, *1* (32), 4908−4915.

(51) Thornburg, D. M.; Madix, R. J. Cleavage of Nh Bonds by Active Oxygen on Ag(110): II. Selective Oxidation of Ethylamine to Acetonitrile. *Surf. Sci.* **1990**, *226* (1), 61−76.

(52) Hu, S.; Tian, R.; Dong, Y.; Yang, J.; Liu, J.; Chang, Q. Modulation and Effects of Surface Groups on Photoluminescence and Photocatalytic Activity of Carbon Dots. *Nanoscale* **2013**, *5* (23), 11665−11671.

(53) Tang, L.; Ji, R.; Cao, X.; Lin, J.; Jiang, H.; Li, X.; Teng, K. S.; Luk, C. M.; Zeng, S.; Hao, J.; Lau, S. P. Deep Ultraviolet Photoluminescence of Water-Soluble Self-Passivated Graphene Quantum Dots. *ACS Nano* **2012**, *6* (6), 5102−5110.

(54) Niu, X.; Li, Y.; Shu, H.; Wang, J. Revealing the Underlying Absorption and Emission Mechanism of Nitrogen Doped Graphene Quantum Dots. *Nanoscale* **2016**, *8* (46), 19376−19382.

(55) Khan, S.; Gupta, A.; Verma, N. C.; Nandi, C. K. Time-Resolved Emission Reveals Ensemble of Emissive States as the Origin of Multicolor Fluorescence in Carbon Dots. *Nano Lett.* **2015**, *15* (12), 8300−8305.

(56) Chaojie Song, J. Z. Electrocatalytic Oxygen Reduction Reaction. In *PEM Fuel Cell Electrocatalysts and Catalyst Layers*; Springer: London, 2008; pp 89−134.

(57) Lv, Q.; Si, W.; He, J.; Sun, L.; Zhang, C.; Wang, N.; Yang, Z.; Li, X.; Wang, X.; Deng, W.; Long, Y.; Huang, C.; Li, Y. Selectively

Nitrogen-Doped Carbon Materials as Superior Metal-Free Catalysts for Oxygen Reduction. *Nat. Commun.* **2018**, *9* (1), 3376.

(58) Liu, Y.; Kim, D. Y. Enhancement of Capacitance by Electrochemical Oxidation of Nanodiamond Derived Carbon Nano-Onions. *Electrochim. Acta* **2014**, *139*, 82−87.